SAE INTERNATIONAL®

Cellular Helmet Liner Design through Bio-inspired Structures and Topology Optimization of Compliant Mechanism Lattices

Joel C. Najmon, DeHart J. Jacob, Zebulun M. Wood, and Andres Tovar, *Indiana University-Purdue University Indianapolis, USA*

Abstract

The continuous development of sport technologies constantly demands advancements in protective headgear to reduce the risk of head injuries. This article introduces new cellular helmet liner designs through two approaches. The first approach is the study of energy-absorbing biological materials. The second approach is the study of lattices comprised of force-diverting compliant mechanisms. On the one hand, bio-inspired liners are generated through the study of biological, hierarchical materials. An emphasis is given on structures in nature that serve similar concussion-reducing functions as a helmet liner. Inspiration is drawn from organic and skeletal structures. On the other hand, compliant mechanism lattice (CML)-based liners use topology optimization to synthesize rubber cellular unit cells with effective positive and negative Poisson's ratios. Three lattices are designed using different cellular unit cell arrangements, namely, all positive, all negative, and alternating effective Poisson's ratios. The proposed cellular (bio-inspired and CML-based) liners are embedded between two polycarbonate shells, thereby, replacing the traditional expanded polypropylene foam liner used in standard sport helmets. The cellular liners are analyzed through a series of 2D extruded ballistic impact simulations to determine the best performing liner topology and its corresponding rubber hardness. The cellular design with the best performance is compared against an expanded polypropylene foam liner in a 3D simulation to appraise its protection capabilities and verify that the 2D extruded design simulations scale to an effective 3D design.

Introduction

In recent years, the short- and long-term effects of sports-related head injuries, like traumatic brain injuries (TBIs) and mild traumatic brain injuries (mTBIs), more commonly referred to as concussions, have become apparent. A recent study from the Boston University Alzheimer's Disease and Chronic Traumatic Encephalopathy (CTE) Center found that 99% of the brains of deceased National Football League (NFL) players (87% across all levels of play) were found to have CTE, which is associated with memory and mood impairments and dementia [1]. Furthermore, athletes who received head injuries in the past are more susceptible to mTBIs, intensifying their effects [2]. These facts show the inadequacies in traditional approaches to helmet design, and call for disruptive technologies to escalate helmet safety and reduce the risk of head injury prone sports.

For single-impact helmets, such as bike, motorcycle, and horse riding helmets, a non-reusable foam liner is used, typically expanded polystyrene (EPS). For multi-impact helmets, such as football, baseball, and ice hockey helmets, the most common liner material is expanded polypropylene (EPP) foam. Special liners in football and motorcycle helmets incorporate viscoelastic polymers such as butyl nitrate and Zorbium, inflatable liners (Riddell SpeedFlex), air shock absorbers (Schutt Air XP Line), and omnidirectional suspension systems (6D Helmets) [3].

The introduction of dynamic, nonlinear finite element solvers has shifted helmet development toward simulation-based design [4, 5, 6]. The availability of supercomputers, advanced design algorithms (e.g., topology optimization), and additive manufacturing offers a unique opportunity to shorten the helmet development cycle and achieve high performance [7, 8]. Recently, several research groups have addressed fundamental design aspects in helmets for football [9, 10, 11], motorcycle [12, 13, 14], and cycling [15, 16]. Interestingly, specialized helmets are being developed for sports such as pole vaulting, soccer, lacrosse, and field hockey [17], as well as new sports activities such as e-bikes, segways, and electric unicycles [18]. While innovative helmet designs have contributed to reducing concussions for many sport practitioners ranging from children to elite athletes [19], there is no "magic" concussion-preventing product on the market at this time, and further developments are needed to cope with ever-evolving sport requirements.

Bio-inspired designs are driven by the desire to capture the outstanding features and performance seen in nature and integrate these benefits into engineering products [20]. Properties of bio-inspired materials tend to surpass properties of many man-made materials making their production and practical application valuable to impact energy absorption [21, 22]. The field of bio-inspired design has greatly advanced in the last decade with the development of new methods and software tools, usually in the form of databases and search engines. Methods include the use of inventive problem-solving theory (BioTRIZ) [23] and functional modeling [24]. Tools include lexical databases [25], online repositories such as AskNature from the Biomimicry Institute (asknature.org), IDEA-INSPIRE [26], and the Design by Analogy to Nature Engine (DANE) [27] as well as repository search algorithms [28]. The study of certain plant structures has shown promise for absorbing impact energy [29]. For example, the porous structure of a pomelo peel is a continued interest in research groups for energy-absorbing applications [30, 31]. Additionally, head impact injury prevention materials and structures can be found in bighorn sheep, muskox, and woodpeckers, among others, inspiring the development of cellular materials for impact energy absorption [29, 32, 33, 34, 35, 36, 37]. For instance, fish and crocodile scales and turtle carapace have inspired the design of flexible armors [36]. The woodpecker's beak and skull, which protect them from injury in spite of repeated impacts, are a subject of study for applications in impact protective systems [37, 38, 39]. However, to date, applications on helmet design remain scarce. In this work, bio-inspired liner designs mimic the organic and skeletal structures found in pomelo peels, nautilus shells, and woodpeckers' skulls.

Engineered cellular materials have been developed for impact energy absorption in the form of honeycombs [40, 41], microlattices [42], hollow spheres [43, 44, 45], and foams [46, 47]; however, these cellular materials lack the ability to predictably redirect an

impacting force and manage energy absorption [48]. In order to address this issue, this work expands on the design of a compliant mechanism lattice (CML) previously introduced by our group [49, 50]. The CML redistributes an incoming radial force to tangential directions [51]. In this work, CML-based liners are developed using topology optimization to synthesize rubber cellular unit cells with effective positive and negative Poisson's ratios. The energy-absorbing capability of the proposed CML-based liners is compared to that of bio-inspired liners [52]. The six proposed cellular liners and an EPP foam liner are through a series of numerical ballistic simulations.

This article is organized as follows: The proposed bio-inspired and CML-based liners are presented in Sections 2 and 3, respectively. Sections 4 and 5 present the finite element impact model and the results of the numerical ballistic simulation on the proposed cellular liners and the EPP foam liner. Conclusions and final remarks are presented in Section 6.

FIGURE 1 Bio-inspired designs: (a) pumpkin, (b) stacked diatom skeletal, (c) internal Fibonacci spiral, (d) haystack, (e) wheel spoke, (f) external Fibonacci spiral, (g) spiral wave, (h) double helix, (i) hexagonal spring.

© Indiana University-Purdue University Indianapolis
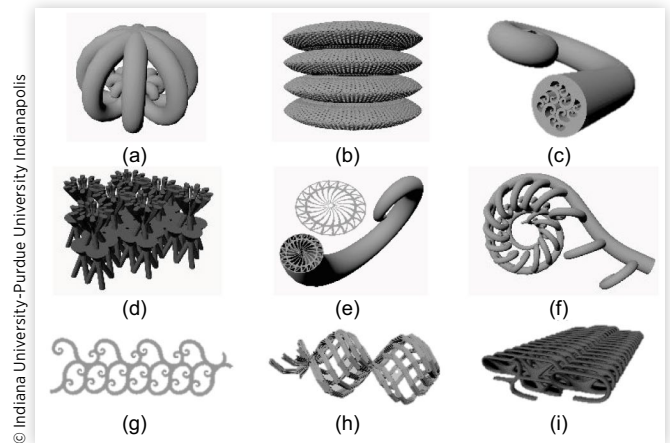
Bio-inspired Design

When investigating protective natural materials, inspiration is drawn from two categories of natural structures. The first category is organic structures from plants that serve similar protection capabilities to that of a helmet liner. For example, citrus fruits, coconuts, and gourds all have peels, shells, and rinds to protect the seeds from impacts and falls from trees.

The second category is skeletal structures that prevent internal penetrations while providing support for cyclical impacts. Design inspiration comes from a wide variety of protective natural materials ranging from macroscopic skeletons of sea life to the hierarchical structure of the bone (Figure 1).

Bio-inspired Design Process

The bio-inspired design process in this work is derived from BioTRIZ [23] and relies on function-form analogies between biological and engineering designs (Figure 2). This process involves identifying the engineering-required function (e.g., TBI mitigation, impact energy absorption), finding the biological analogous function and the corresponding biological form (e.g., cellular material), and translating it into an engineering form.

In this work, the exploration of the available tools and repositories, particularly AskNature, and the biological form-function analogies led to the definition of structural tissue as the biological material for liner inspiration. Examples of biological and engineering forms are shown in Figure 3.

Focus is given to material with hierarchical structures of varying densities. Despite the bio-inspired designs having varying local density, the overall designs are developed with a 40% volume fraction constraint, for fair comparison with the CML-based liners. Three bio-inspired designs are developed, namely, peel, shell, and bone designs as described below.

Peel Design

The peel design is inspired on the peel of the pomelo fruit (Figure 4). The pomelo is a large citrus (20 cm in diameter and 2 kg in mass) that grows on tall trees (10 m). In free-fall tests, pomelos showed that their peel constitutes an impact protection layer that prevents the fruit from splitting open when impacting on the ground after being shed [53].

FIGURE 2 Flowchart of the bio-inspired design process.
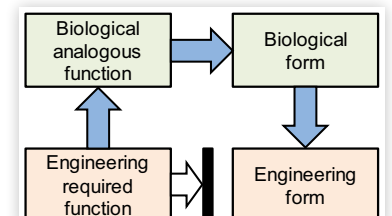
© Indiana University-Purdue University Indianapolis

**FIGURE 3** Example of a bio-inspired design: biological form of a diatom skeletal remains under an electron microscope (left) and the corresponding engineering form (right) reproduced in Zbrush.
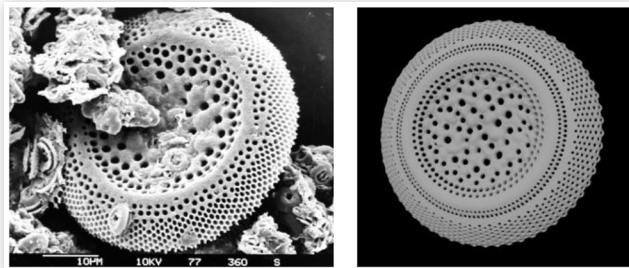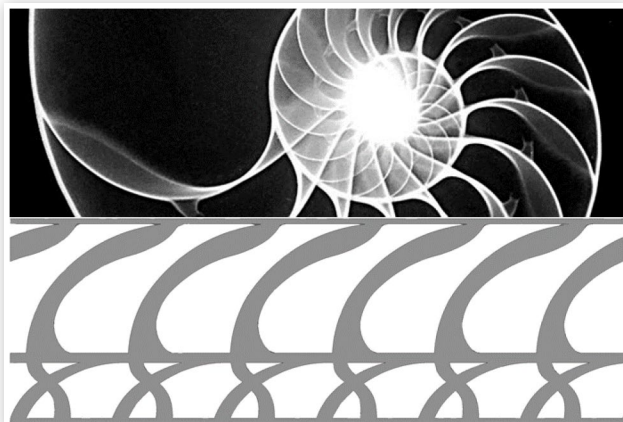

© Indiana University-Purdue University Indianapolis

FIGURE 4 Section of 1 × 3 cellular unit cells of the peel design (bottom) inspired by the dense and porous layers (exocarp and mesocarp) of a pomelo peel (top) [54].
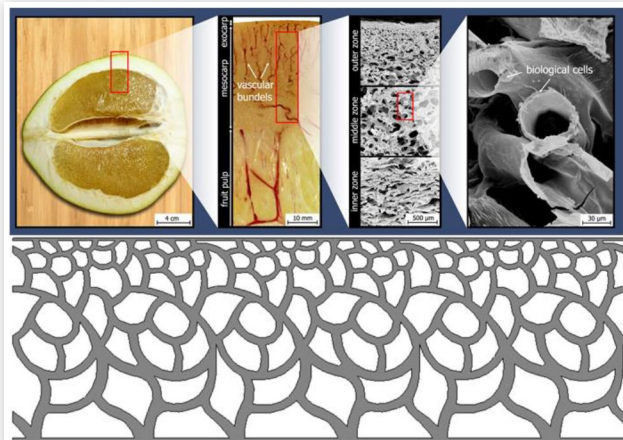
© Indiana University-Purdue University Indianapolis

FIGURE 5 Section of 1 × 3 cellular unit cells of the shell design (bottom) inspired by the cross-sectional topology of a nautilus shell (top).

© Indiana University-Purdue University Indianapolis

The pomelo peel is characterized by two distinct layers: the exocarp and the mesocarp. The exocarp (outer layer) is densely packed and forms the skin of a pomelo. The mesocarp (inner layer) is a porous structure. The bio-inspired peel design attempts to capture the penetration resistance offered by the outer dense layer, while allowing the porous inner layer to deform as it absorbs energy [54].

Shell Design

This design is inspired by the cross-sectional structure of a nautilus shell (Figure 5). Nautilus shells are highly resilient structures with the ability to withstand enormous water pressures at depths of 800 m [55]. The bio-inspired shell design mimics the crisscrossed inner structure of the nautilus shell with an outer layer comprised of long arches (septa). The septa allow for a gradual deceleration of an impact, while the inner interlocking arches prevent extreme deformations.

Bone Design

This design is inspired by the internal structure of the cranial bone found in the skull of woodpeckers (Figure 6). In conjunction with other biomechanical features, their internal bone structure is able to absorb high impact energy, which allows woodpeckers to drum on trees more than 10 times every second (12,000 times a day) [37]. The speed of the head in each drum is 7 m/s and experiences decelerations of 1,000 g without experiencing brain injuries [37].

The bone internal architecture features two dense plates of compact bone that sandwich a relatively thick section of spongy bone. The lightweight spongy bone absorbs impact energy, while the compact bone provides penetration resistance and structural rigidity. Compared to other bird skulls, the woodpecker's skull has a larger portion of spongy bone. When forces reach the spongy bone, its structure disperses them in divergent tangential directions away from the axis of impact [38]. This desirable force redirection is to be achieved with a compliant mechanism lattice-based design and the use of topology optimization as described in the following section.

Compliant Mechanism Lattice-Based Design

Optimization Problem Statement

Engineered cellular materials have the potential to be low volume and lightweight while providing low peak acceleration, low displacement, and high energy absorption. In this work, a topology optimization algorithm is used to synthesize

a compliant mechanism cellular unit cell that comprises the CML-based liner. The algorithm operates through the use of solid isotropic material with penalization (SIMP) to perform density-based topology optimization [56].

The compliant mechanism design problem is defined as finding the density distribution $\mathbf{x} \in \mathbb{R}^n$ in a discretized design domain of the cellular unit cell that maximizes the mutual potential energy (MPE) resulting from the application of input and output loads. The maximization of MPE maximizes the displacement of the output nodes for a given input force. The optimization problem is subjected to a volume fraction constraint $v(\tilde{\mathbf{x}}(\mathbf{x}))$, and it is mathematically expressed as

FIGURE 6 Section of 1 × 3 cellular unit cells of the bone design (bottom) inspired by the sandwich of (a) compact and (b) spongy bone found in a woodpecker's skull (top) [37].

© Indiana University-Purdue University Indianapolis

$$\text{find} \quad \mathbf{x} \in \mathbb{R}^n$$
$$\max \quad \text{MPE}\big(\tilde{\mathbf{x}}(\mathbf{x})\big) = \mathbf{U}\big(\tilde{\mathbf{x}}(\mathbf{x})\big)_{\text{in}}^{\text{T}} \mathbf{K}\big(\tilde{\mathbf{x}}(\mathbf{x})\big) \mathbf{U}\big(\tilde{\mathbf{x}}(\mathbf{x})\big)_{\text{out}}$$
$$\text{s.t.} \quad v\big(\tilde{\mathbf{x}}(\mathbf{x})\big) = \mathbf{v}^{\text{T}}\tilde{\mathbf{x}}(\mathbf{x}) = \sum_{i=1}^{n} v_i \tilde{x}_i(x_i) \leq \overline{v}$$
$$\mathbf{x} \in \chi, \quad \chi = \big\{\mathbf{x} \in \mathbb{R}^n : 0 \leq x_i \leq 1,\ i=1,\ldots,n\big\}, \qquad \text{Eq. (1)}$$

where $\overline{v}$ is a volume fraction limit and v_i is the element volume. In (1), $\tilde{x}_i(x_i)$ is the filtered variable defined by

$$\tilde{x}_i(x_i) = \frac{\sum_{j \in N_i} H_{ij} v_j x_j}{\sum_{j \in N_i} H_{ij} v_j}, \qquad \text{Eq. (2)}$$

where H_{ij} is a weight factor and N_i is the neighborhood of the element x_i with a filter radius R, or $N_i = \{j : \text{dist}(i,j) \leq R\}$. In (1), $\mathbf{U}\big(\tilde{\mathbf{x}}(\mathbf{x})\big)_{\text{in}}$ and $\mathbf{U}\big(\tilde{\mathbf{x}}(\mathbf{x})\big)_{\text{out}}$ represent the vector of nodal displacements resulting from the application of the input and output loads, respectively. $\mathbf{K}\big(\tilde{\mathbf{x}}(\mathbf{x})\big)$ is the stiffness matrix resulting from the SIMP interpolation

$$\mathbf{K}\big(\tilde{\mathbf{x}}(\mathbf{x})\big) = \sum_{i=1}^{n} \Big[E_{\text{min}} + \tilde{x}_i^p \big(E_0 - E_{\text{min}}\big) \Big] \mathbf{K}_i^0, \qquad \text{Eq. (3)}$$

where $\mathbf{K}_i^0$ is the (constant) extended element stiffness matrix corresponding to a unit value of the design variable, E_0 is the Young's modulus of the base material, E_{min} is a Young's modulus lower bound ($E_{\text{min}} = E_0 \times 10^{-6}$), and p is the penalization power. The sensitivity coefficients of MPE in (1) are obtained using direct differentiation [56]. The optimization problem is numerically solved using the method of moving asymptotes (MMA) [57].

Compliant Mechanism Designs

There are two primary designs of compliant mechanisms for use in the CML-based liner. Both function by redirecting an incoming radial force to a tangential direction. The first design for the compliant mechanism redirects forces out from the point of impact. Holistically, this gives the compliant mechanism an effective positive Poisson's ratio; therefore, it is referred to as *the positive mechanism*. The second design redirects the incoming force inward, translating to an effective negative Poisson's ratio for the mechanism; therefore, it is referred to as the *negative mechanism*.
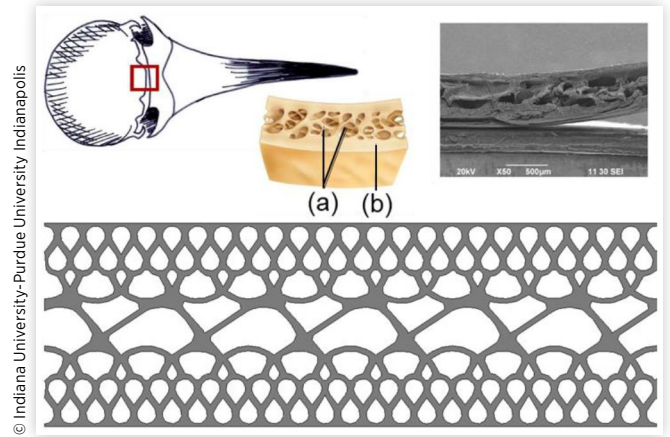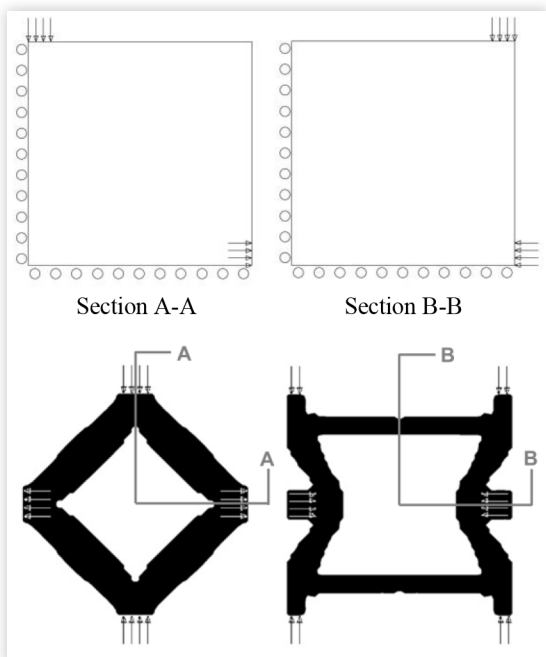
By applying symmetric boundary conditions, only one-quarter of the mechanism needs to be optimized. Each problem is run with a 30 × 30 element mesh. For the positive mechanism, an input load is specified in the upper left corner and a (dummy) output load is specified in the lower right corner of the design domain. Similarly, for the negative mechanism, an input load is defined in the upper right corner with a (dummy) output load specified in the lower right corner of the design domain. Each load is given a width of 10% of the edge length, to achieve a large enough connection area so that liner implementation is robust. Roller supports are applied to the nodes along the left and bottom edges of the design domain for both mechanisms. Figure 7 shows section views of the loaded nodes, load orientations, and supports for the positive and negative mechanisms.

By performing topology optimization on the compliant mechanism problems, a 2D topology is obtained, which can be extruded for performance analysis in LS-DYNA. The volume fraction is set to $\bar{v} = 0.40$ in (1). A filter radius $R = 3.0$ elements in (2) is also added to prevent the creation of spindly members. The SIMP penalization power is set to a value of $p = 3.0$ in (3). Figure 7 shows the resulting cellular unit cell topologies for the positive and the negative mechanisms. Each cellular unit cell is 19.05 mm × 19.05 mm (0.75″ × 0.75″). Three-dimensional versions of the compliant mechanisms are synthesized using the optimization tool top3d for Matlab (top3dapp.com) [56] (Figure 8). Due to the computational cost associated with 3D CML-based liner simulations, the numerical model for analysis and comparison of liners is done with 2D extruded topologies as described in the next section.

Numerical Model

Probable Contact Area

To determine a suitable liner width and the corresponding number of cellular unit cells, a simulation of the National Operating Committee on Standards for Athletic Equipment (NOCSAE) helmet drop test [58] is analyzed. For this simulation, a full-sized helmet is designed along with the model of the NOCSAE headform (Figure 9). The helmet has a polycarbonate outer shell (2.0 mm thickness) and impact absorbent EPP foam pads (approx. 19 mm thick). The NOCSAE headform model is made of magnesium and is dropped in free fall onto a 12.7 mm thick modular elastomer programmer (MEP) test pad made of molded polyurethane. From this simulation, it is found that the projected impact area of the 4.9 kg headform moving at 5.46 m/s is approximately an oval with a major axis of 85 mm and a minor axis of 80 mm. In order to ensure that the liner model is long enough to suitably capture deformations at its boundary, 9 unit cells are selected for the model to have a total width of 171.5 mm, which covers over twice the length of the impact area's major axis. The 3D simulation liner is not oversized, resulting in a liner that is 5 × 5 unit cells.

Liner Assembly

The bio-inspired and the CML-based liners, with a thickness of 19.05 mm, are assembled between two polycarbonate shells, with a thickness of 2.0 mm. The total width of the 2D liners is 171.5 mm with an extruded depth of 5 mm. The resulting overall dimensions of the 2D liners are 23.05 mm × 171.5 mm × 5.0 mm.

FIGURE 7 Optimized topologies of the positive mechanism (left) and the negative mechanism (right) with corresponding section views of loads and boundary conditions of a quarter design domain.

Section A-A   Section B-B

© Indiana University-Purdue University Indianapolis

Three bio-inspired liners (the peel, shell, and bone liners) are shown in Figure 10. Three CML-based liners are shown in Figure 11, consisting of (i) all positive mechanisms, (ii) all negative mechanisms, and (iii) alternating positive and negative mechanisms. The liners with the all positive, all negative, and alternating positive and negative mechanisms are referred to as the *positive liner* (PL), *negative liner* (NL), and net *zero liner* (ZL), respectively.

Simulation Setup

Each liner model is put through a numerical ballistic simulation using LS-DYNA. A polycarbonate impactor is modeled as a rigid shell cylinder with a depth of 5.0 mm, diameter of 100 mm, and mass of 70 g. The diameter corresponds to the top diameter of a medium NOCSAE headform. The mass of 70 g is conducive to observing liner deformation matching the NOCSAE Drop Test (Figure 9)-an impactor with this mass does not under-deform or over-deform the 2D extruded liners. The rigid cylinder impacts the top surface of the liner at 5 mm/ms. The side surface nodes are supported with rollers. A 12.7 mm thick MEP test pad, with a fixed bottom support, is placed underneath the liner. The soft pad allows the inner shell to deform (for performance evaluation), while still grounding the impact. Figure 12 shows the initial 2D ballistic simulation setup for analysis of the PL design.

Model Details

The polycarbonate shells are modeled as a linear elastic solid [49, 50]. The model of the bio-inspired liners has their top and bottom surfaces attached to the adjacent sides of the outer and inner shells, respectively. The model of the CML-based liners has their compliant mechanisms attached to each other at their respective output ports and to the outer and inner shells at their respective input ports.

The MEP test pad and liners are both modeled with the two-parameter incompressible Mooney-Rivlin rubber model [59],

$$W = A(I_1 - 3) + B(I_2 - 3) + C\left(\frac{1}{I_3^2} - 1\right) + D(I_3 - 1)^2, \qquad \text{Eq. (4)}$$

where W is the strain energy function and I_1, I_2, and I_3 are deviatoric strain invariants of the Cauchy-Green tensor and

$$C = \frac{1}{2}A + B, \quad D = \frac{A(5v - 2) + B(11v - 5)}{2(1 - 2v)},$$

where v is the Poisson's ratio. The material parameters A and B are user-defined constants. In this work, these parameters are obtained from experimental data as a function of the rubber Shore A hardness [60]. Shore A hardness is a measure of the hardness of the material, using the type A scale, typical for softer materials.

FIGURE 8 Three-dimensional optimized topologies of positive (top) and negative (bottom) mechanisms.

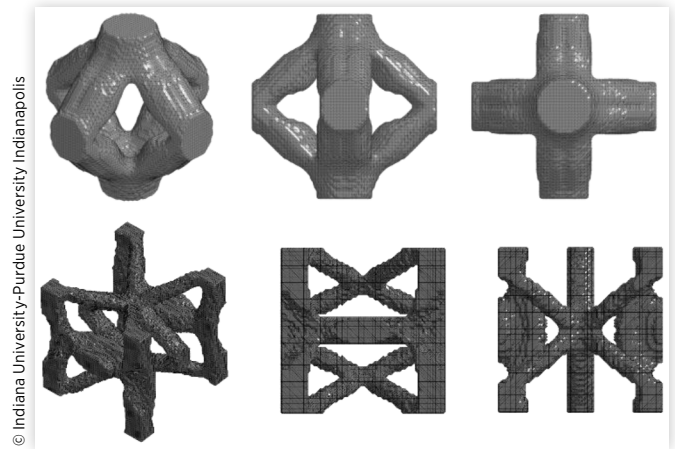© Indiana University-Purdue University Indianapolis

FIGURE 9 Simulation of NOCSAE Drop Test Method ND 001 on a basic foam-based helmet to determine width of (top side) impact area.

85 mm

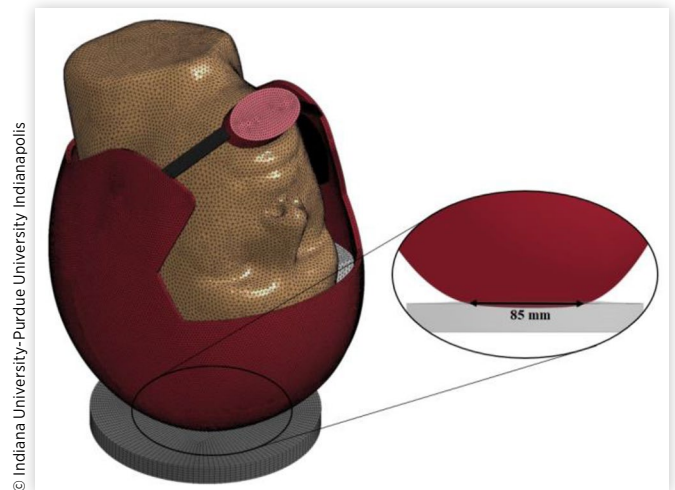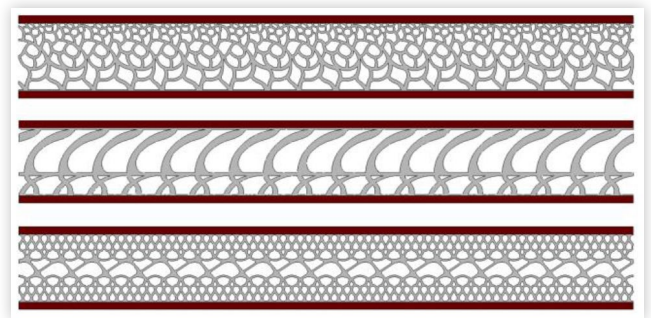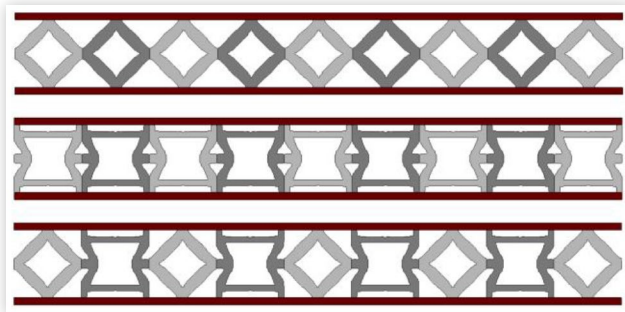© Indiana University-Purdue University Indianapolis

FIGURE 10 Bio-inspired liner assemblies: peel liner (top), shell liner (middle), and bone liner (bottom).
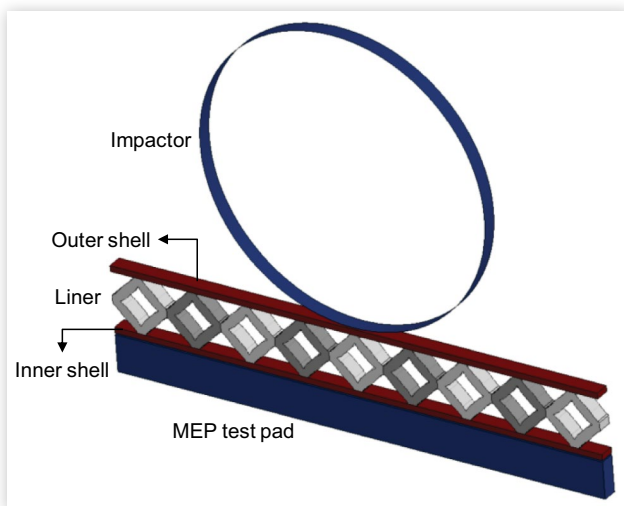

© Indiana University-Purdue University Indianapolis

FIGURE 11 CML-based liner assemblies: positive liner PL (top), negative liner NL (middle), and zero liner ZL (bottom).

© Indiana University-Purdue University Indianapolis

FIGURE 12 2D ballistic simulation setup for the positive liner (PL) design.

© Indiana University-Purdue University Indianapolis

Rubber was chosen as the principle material for this investigation for two main reasons: First, rubbers are commercially available in a wide range of Shore A hardness values. Second, surrogate rubber materials used in this work are also available for material jetting (PolyJet) additive manufacturing, which allows the rapid prototyping of liner designs with complex geometries [61].

For the baseline simulation, LS-DYNA's low density foam model is used to model EPP foam [62]. Simulation variables not dependent on liner type and rubber hardness are kept consistent across all ballistic simulations. This includes timestep options, hourglass control, contact definitions, initial velocities, boundary conditions, element formulations, and other model options. The complete LS-DYNA material model keycard details can be found in the Appendix.

Performance Evaluation Criteria

It is well established that TBIs and mTBIs are linked with the linear and rotational accelerations experienced by the brain [63]. Consideration of injurious accelerations is evaluated to assess the protective capabilities of the bio-inspired and CML-based liners. In this work, four related performance evaluation criteria are utilized:

a_{max}: peak acceleration of the impactor (g)
HIC_{15}: head injury criterion (HIC) at 15 ms
d_{max}: peak displacement of the inner shell (mm)
PIE_{sd}: standard deviation of peak internal energy (PIE) distribution within the liner (mm)

The first evaluation criterion is the peak acceleration of the impactor's center of mass,

$$a_{max} = \left\{ |a(t)| \right\}_{max},$$ Eq. (5)

which is also proportional to the maximum force experienced as a result of the impact but does not fully capture its severity. Notably, a steep spike to a low peak acceleration can be just as detrimental as a gradual rise to a high peak acceleration [64] and, therefore, the HIC is employed to capture the significance of the slope of a resultant acceleration curve [65]. In particular, the HIC measures the likelihood of a head injury resulting from an impact using the following time integral:

$$HIC = \left\{ (t_2 - t_1) \left[\frac{1}{(t_2 - t_1)} \int_{t_1}^{t_2} a(t) dt \right]^{2.5} \right\}_{max},$$ Eq. (6)

where $a(t)$ is the impactor's acceleration in g (gravity) and t_1 and t_2 are the initial and final times (in seconds) of the time interval that maximizes HIC.

This work uses HIC_{15}, which sets the integral's time interval to 15 ms as follows:

$$HIC_{15} = \left\{ (0.015)^{1.5} \left[\int_{t_1}^{t_1+0.015} a(t) dt \right]^{2.5} \right\}_{max}.$$ Eq. (7)

TABLE 1 Pairwise comparison table for weight calculation.

f	Pairwise comparison						Σ	ω
a_{max}	1	2	1.5				4.5	0.25
HIC_{15}	2			2	2		6.0	0.33
d_{max}			1.5		1	2	4.5	0.25
PIE_{sd}		1		1		1	3.0	0.17
Σ	3	3	3	3	3	3	18.0	1.00

As a reference, when HIC15 = 1000, there is 18% probability of severe head injury, 55% probability of serious head injury, and 90% probability of a moderate head injury, for the average human [66]. However, the ballistic simulation in this study does not accurately model impact on a human head; consequently, HIC_{15} values in this article are used exclusively for comparison purposes.

The third performance criterion is the peak displacement d_{max} seen by the inner shell's center of mass. Deformations on the inside of the liner should be kept to a minimum, as they lead to increased risk of head injury.

The last performance criterion quantifies internal energy distributions. For all liners, the maximum internal energy is obtained at the peak displacement of the impactor. At this point, a suitable evaluation criterion is the PIE distribution among the cellular unit cells, which is evaluated through its standard deviation,

$$\text{PIE}_{sd} = \sqrt{\frac{1}{N}\sum_{I=1}^{N}\frac{\left(X_i - \bar{X}\right)^2 \text{PIE}_i}{\text{PIE}_{total}}} \qquad \text{Eq. (8)}$$

where N is the number of unit cells, X_i is the position of the ith unit cell, $\bar{X}$ is the average unit cell position ($\bar{X} = 0$), PIE_i is the internal energy of the ith unit cell at peak displacement, and PIE_{total} is the total internal energy of the unit cells at peak displacement. For 3D simulations, the expression $\left(X_i - \bar{X}\right)$ in (8) is replaced with the distance between the ith unit cell and the average unit cell position.

To aid with the evaluation of the liner, performance values are normalized. A subsequent weighted sum is calculated and used for justification of selecting designs for further analysis. The resulting weighted score is then defined as

$$\text{WS} = \sum_{j=1}^{4}\omega_j\frac{f_j - f_{min}}{f_{max} - f_{min}} = \sum_{j=1}^{4}\omega_j\bar{f}_j, \qquad \text{Eq. (9)}$$

where $\bar{f}_j$ is the normalized performance value and ω_j the corresponding weight. Since all of the performance values (except PIE_{sd}) are desired to be minimized, the best design is the one with the lowest weighted score. For consistency with the other criteria, higher PIE_{sd} values are assigned lower normalized performance values. The weights ω_j are decided by the pairwise comparison method [67] where one assigns relative value to matched pairs (Table 1).

Numerical Results

The performance of the bio-inspired and CML-based liners is determined through two series of ballistic simulations on the 2D-extruded designs. The first series of simulations shows the liner designs with Shore 60A rubber, which are referred to as the *basic* liners in this work. From these simulations, the bio-inspired and CML-based liners with the lowest weighted scores are selected to go through a second series of

FIGURE 13 Deformation at peak displacement of the inner shell for (a) peel liner (d_{max} = 1.6 mm), (b) shell liner (d_{max} = 2.8 mm), (c) bone liner (d_{max} = 1.9 mm), (d) positive liner PL (d_{max} = 1.9 mm), (e) negative liner NL (d_{max} = 1.4 mm), and (f) zero liner ZL (d_{max} = 2.8 mm) (MEP test pad hidden for clarity).
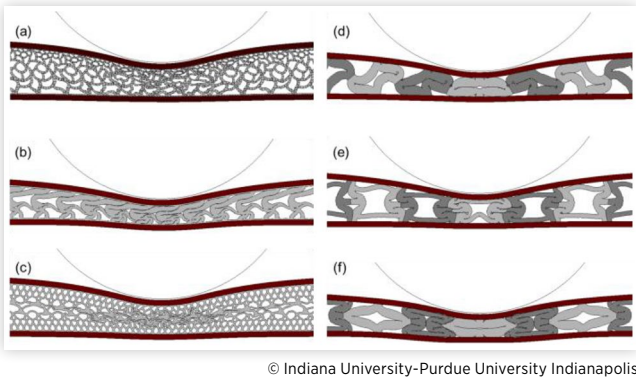
© Indiana University-Purdue University Indianapolis

FIGURE 14 Displacement-acceleration and time-acceleration profiles of the six (basic) liners using Shore 60A rubber.
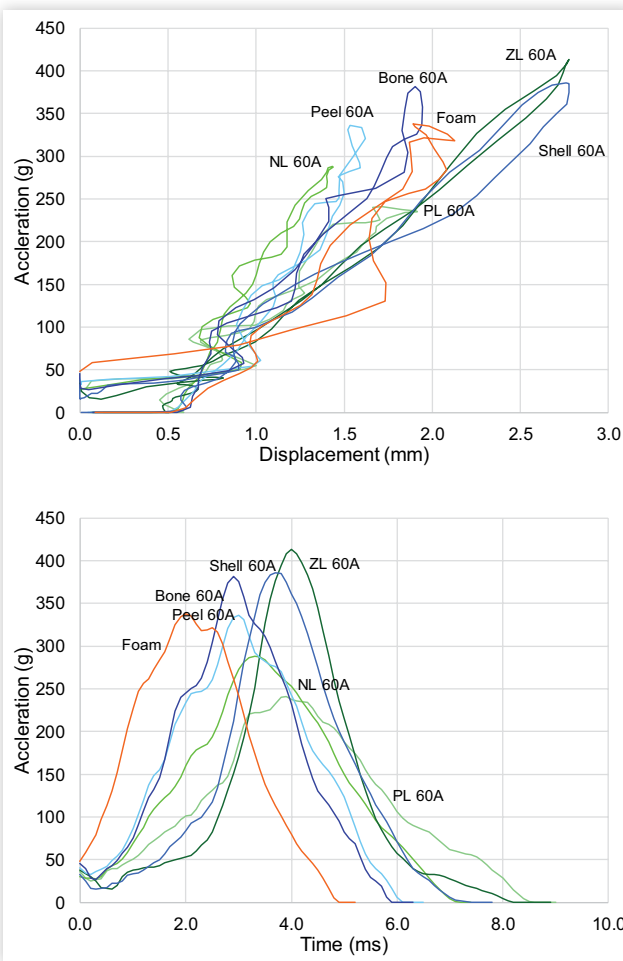
simulations consisting of a parametric study of Shore A rubber hardness, from 40A to 80A. For comparison, a traditional EPP foam liner is also evaluated. A final 3D numerical ballistic simulation compares the best performing liner against the EPP foam liner.

Performance of the Basic Liners

The numerical performance study of the six basic liners shows the effect of the liners' topology on their performance. Observing Figure 13, the peel and bone liners see significant improvement in inner shell displacement compared to the shell liner. This is due to the highly complex dense regions in these liners that resist transverse loads. Even though the shell liner does have a relatively dense region, it is comprised of long spindly arches which buckle in an ineffective manner. On the other hand, it can be seen that the PL and NL resisted internal shell deformations despite undergoing severe crushing of the liner. The ZL saw a similar level of crushing, yet suffered extreme inner shell displacement. From this analysis, the d_{max} of the inner shell is inversely proportional to the internal forces (tensile or compressive) that are present in the liner. The peel, bone, PL, and NL liners all saw relatively low d_{max} values, due to the large conflicting forces seen in their dense regions and conflicting mechanism outputs. The spiral and ZL liners did not have these features resulting in greater displacement of the inner shell.

The displacement-acceleration profiles (Figure 14) at a glance are noisy. This is due to the acceleration and displacement being measured independently at the impactor and inner shell, respectively. The vibration experienced in each of the bodies is delayed by the thick section of rubber liner in-between them. While this makes the profiles hard to read, the peaks of the profiles can still clearly be seen, which shows the relationship of the impactor's acceleration and inner shell's displacement among the liners.

When comparing the displacement-acceleration profiles of Figure 14, the EPP foam liner is dominated by the peel, PL, and NL liners. These designs have topologies that stretched and compressed under a transverse load, absorbing impact energy as strain energy. The shell and ZL liners offered little internal resistance during impact, resulting in extreme bending of the inner shell (Figure 13) and high peak accelerations. The ZL's performance is specifically due to lack of straining between adjacent positive and negative mechanisms. In the PL and NL liners, the output ports apply a compressive and tensile load (respectively) on their members, converting kinetic energy to strain energy. In the ZL, input and output ports move together, collapsing the structure with limited strain and thus limited energy absorption.

The PIE for the nine unit cells is shown in Figure 15. The PIE tends to be more concentrated in the middle unit cell for the geometrically complex peel, bone, and NL liners. The geometrically simple shell, PL, and ZL liners

show similar PIE distribution, with the middle three unit cells absorbing near equal levels of internal energy, resulting in the three highest PIE$_{sd}$ in Table 2. The geometrically simple topologies of these liners result in a more uniform deformation across the unit cells (Figure 13), resulting in a more uniform PIE distribution.

The performance criterion values for the analysis of the basic liners are shown in Table 2. The normalized performance values are shown in brackets with the smallest normalized performance values shaded for each performance evaluation criterion (blue for bio-inspired liners, green for CML-based liners). It is shown that the peel liner has the lowest weighted score of the bio-inspired liners, while the PL has the lowest weighted score of the CML-based liners. The parametric rubber hardness study is performed on these two liners.

FIGURE 15 PIE as a function of the horizontal position of the unit cells for the bio-inspired and CML-based (basic) liners using Shore 60A rubber.
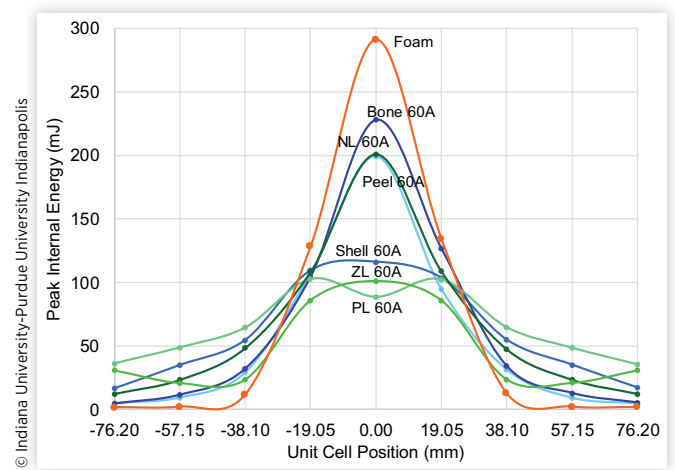
Parametric Study

Rubber hardnesses for the parametric study are chosen depending on the trending improvement in liner performance. The peel liner is analyzed with rubber hardnesses of 40A, 50A, 60A, and 70A, while the PL is analyzed with rubber hardnesses of 50A, 60A, 70A, and 80A. The resulting displacement-acceleration profiles are shown in Figure 16. The peel liner features a rather counterintuitive trend, where the, normally conflicting, a_{max} and d_{max} performance values both improve given a decrease in rubber hardness. Softening the rubber to 40A hardness brings significant improvements in not just the a_{max} and d_{max} but also the HIC$_{15}$ and PIE$_{sd}$ of the liner, as seen in Table 3.

Interestingly, the CML-based PL shows a similar relationship whereas the rubber hardness increases, the new liners dominate the prior liner. This relationship continues until an ideal rubber hardness of 70A is found for the PL. According to the displacement-acceleration profiles of Figure 16, the EPP foam liner design is dominated by most of the PLs and the peel liner with 40A rubber.

Figure 17 shows that an increasing rubber hardness has a negative effect in the distribution of the PIE for both the peel and PL liners, that is, lower PIE$_{sd}$. For the CML-based PL, the relation between rubber hardness and PIE$_{sd}$ is not monotonic, with the highest PIE$_{sd}$ values observed for PL 70A.

TABLE 2 Performance *[normalized]* values for the analysis of basic liners.

f	Basic Bio-inspired liners (60A)			Basic CML-based liners (60A)			EPP	ω
	Peel	**Shell**	**Bone**	**Positive**	**Negative**	**Zero**	**foam**	
a_{max} (g)	336.0	386.1	381.7	240.9	288.4	413.2	337.5	*0.25*
$[\bar{a}_{max}]$	*[0.552]*	*[0.843]*	*[0.817]*	*[0.000]*	*[0.276]*	*[1.000]*	*[0.561]*	
HIC$_{15}$	247.7	303.7	287.6	190.4	221.0	328.7	275.5	*0.33*
$[\overline{HIC}_{15}]$	*[0.414]*	*[0.819]*	*[0.703]*	*[0.000]*	*[0.221]*	*[1.000]*	*[0.615]*	
d_{max} (mm)	1.6	2.8	1.9	1.9	1.4	2.8	2.1	*0.25*
$[\bar{d}_{max}]$	*[0.135]*	*[0.999]*	*[0.378]*	*[0.356]*	*[0.000]*	*[1.000]*	*[0.514]*	
PIE$_{sd}$ (mm)	7.9	11.6	7.9	13.7	9.9	12.8	5.5	*0.17*
$[\overline{PIE}_{sd}]$	*[0.707]*	*[0.253]*	*[0.706]*	*[0.000]*	*[0.468]*	*[0.106]*	*[1.000]*	
WS	0.429	0.774	0.651	0.089	0.221	0.848	0.642	--

FIGURE 16 Displacement-acceleration and time-acceleration profiles for the parametric study of the peel (40A-70A), PL (50A-80A), and foam liners.
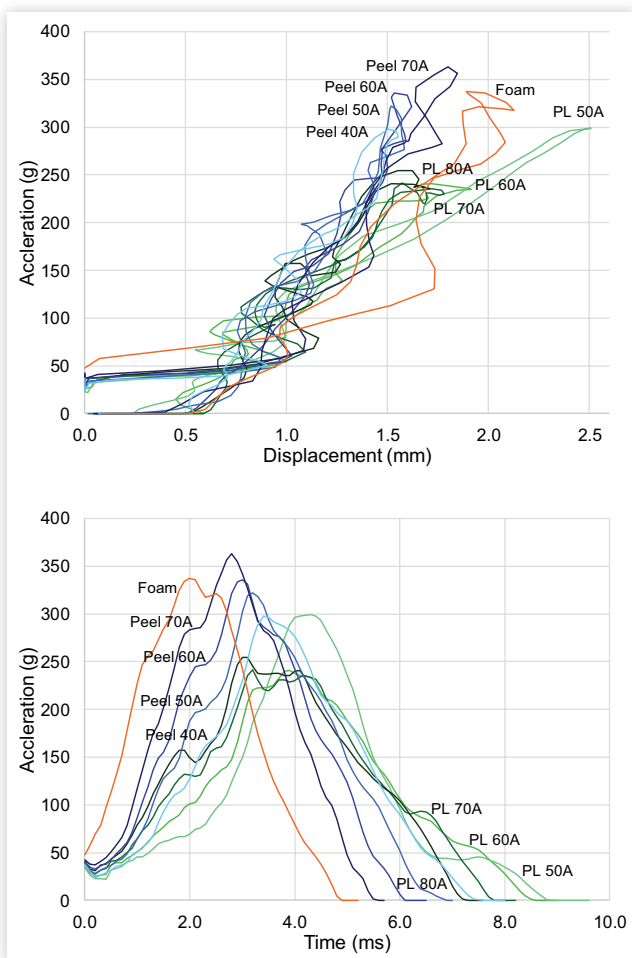

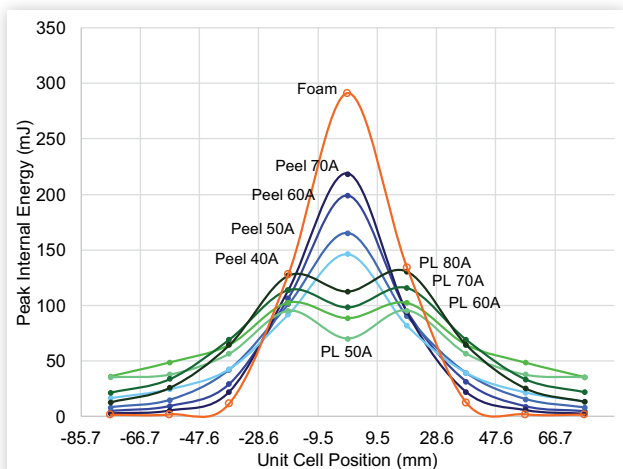© Indiana University-Purdue University Indianapolis

Table 3 shows that the peel liner with 40A rubber and the PL with 70A rubber have the lowest weighted scores for the parametric study of rubber hardness. The liner with the best performance is indicated by the lowest weighted score. Overall the PL with 70A rubber is the best liner from these two series of 2D extruded ballistic simulations.

3D Simulation

An equivalent 3D model (Figure 18) is created to evaluate the CML-based PL. The model tested has dimensions of 5×5 unit cells for a total of 25 positive mechanisms (Figure 8). The mass of the impacting sphere is increased to keep the same mass ratio between impactor and liner as in the 2D models. All other dimensions, material keycards, and contact info are kept consistent with the 2D models.

The 3D ballistic simulation shows the deformation of a 3D positive mechanism when given freedom to buckle out-of-plane. Most of the buckling occurs near the top and bottom of the mechanisms forming the crisscross deformation of the PL design seen in Figure 19. This deformation mode propagates through all of the lattice reaching the mechanisms on the edge.

Observing the transition of the performance values from the 2D to 3D simulations (Table 4), it can be seen that the PL 70A liner maintains a better performance than the EPP foam liner in PIE_{sd} criterion, which means the energy distribution is still better.

The acceleration-based criteria, a_{max} and HIC_{15}, are significantly better in the PL 70A liner compared to the EPP foam liner; however, this compromises the performance with an increased d_{max} value. This is the effect of prescribing displacements in different directions in the liner from discrete locations on the shells. The compromised displacement-acceleration performance can be observed in Figure 20.

FIGURE 17 PIE as a function of the horizontal position of the unit cells for the parametric study of the peel, PL, and foam liners.

© Indiana University-Purdue University Indianapolis

Conclusion

In this work, six cellular liners are designed and analyzed: three bio-inspired designs and three compliant mechanism lattice (CML)-based designs. The bio-inspired designs (peel, shell, and bone) are generated from studying selected energy-absorbing structures from nature that functioned similarly to the role of a helmet liner, namely, pomelo fruit, nautilus shell, and woodpecker's skull. The three CML-based designs (PL, NL, and ZL) are generated using the topology optimization and assembly of CMLs with positive, negative, and zero effective Poisson's ratios. The bio-inspired and CML-based liners were developed with a volume fraction of 40% using rubber as the primary material.

TABLE 3 Performance *[normalized]* values for the parametric study of rubber hardness.

f	Peel liner				Positive liner				EPP foam	ω
	40A	50A	60A	70A	50A	60A	70A	80A	foam	
a_{max} (g)	297.8	322.1	336.0	362.8	298.9	240.9	241.6	254.5	337.5	0.25
$[\bar{a}_{max}]$	[0.467]	[0.666]	[0.780]	[1.000]	[0.476]	[0.000]	[0.006]	[0.111]	[0.793]	
HIC_{15}	303.6	235.4	247.7	277.6	239.9	190.4	182.8	187.2	275.5	0.33
$[\overline{HIC_{15}}]$	[0.410]	[0.554]	[0.684]	[1.000]	[0.602]	[0.080]	[0.000]	[0.046]	[0.978]	
d_{max} (mm)	1.6	1.6	1.6	1.8	2.5	1.9	1.8	1.7	2.1	0.25
$[\bar{d}_{max}]$	[0.000]	[0.033]	[0.070]	[0.307]	[1.000]	[0.380]	[0.240]	[0.164]	[0.603]	
PIE_{sd} (mm)	10.9	9.4	7.9	6.9	13.8	13.7	12.1	10.7	5.5	0.17
$[\overline{PIE_{sd}}]$	[0.357]	[0.538]	[0.711]	[0.838]	[0.000]	[0.016]	[0.210]	[0.372]	[1.000]	
WS	0.313	0.449	0.559	0.799	0.568	0.124	0.097	0.147	0.841	--

This study develops performance evaluation criteria for impact energy-absorbing system analysis, showcases the design of novel bio-inspired and CML-based liners, and compares the performance of the novel liners with traditional EPP foam liners. Numerical simulations are utilized to evaluate the liners' performance in terms of peak acceleration of the impactor (a_{max}), head injury criterion (HIC_{15}), peak displacement of the inner shell (d_{max}), and standard deviation of peak internal energy distribution within the liner (PIE_{sd}). Pairwise comparison is utilized to weight these performance values and evaluate the performance of each design. The results of the simulations are analyzed to establish their relative performance of the liner designs.

The first series of simulations analyze the basic liner topologies with 60A rubber. It is observed that a liner's performance is proportional to the internal in-plane forces present when struck transversely, as seen in the peel liner and PL. Additionally geometrically simple designs (PL, NL, ZL, and shell) have the highest PIE_{sd} values and thus a more uniform deformation across unit cells. From the basic simulations (Shore 60A), the best performing bio-inspired and CML-based designs are the peel liner and the PL, respectively.

A parametric study on Shore A hardness (40A to 80A) is performed on the peel and the PL designs. This study shows that a liner's displacement-acceleration performance can be tuned with the rubber hardness. The best performance of the peel design is obtained with 40A rubber, while the best performance of the PL design is obtained with 70A rubber. Overall, the PL design with 70A rubber is the best performing liner as demonstrated in 2D and 3D simulations and corresponding comparisons with the traditional EPP foam liner.

Research is ongoing to address limitations of this investigation in terms of design and analysis. The computational cost of 3D simulations makes the performance evaluation of 3D (complex) design cumbersome, even in relatively small samples of a helmet liner. To address this issue, homogenization methods are being incorporated to reduce the computational cost of 3D simulations and make it feasible to incorporate design optimization algorithms and evaluate larger

FIGURE 18 3D ballistic simulation setup for the PL design.
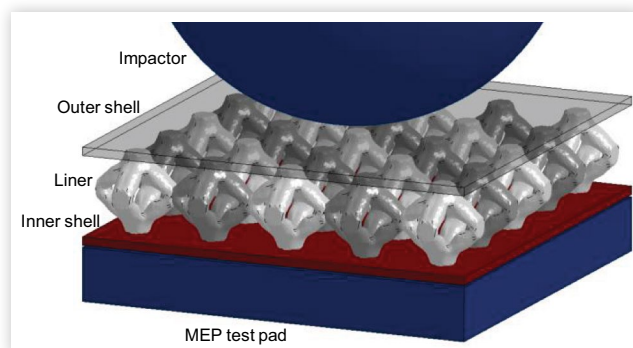
FIGURE 19 Deformation of the 3D PL with 70A rubber at peak displacement of the impactor.
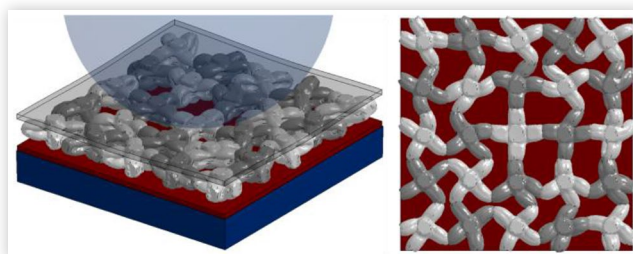
TABLE 4 Performance values of the 2D and 3D liners.

f	2D		3D	
	PL 70A	**EPP foam**	**PL 70A**	**EPP foam**
a_{max} (g)	241.6	337.5	211.9	431.7
HIC_{15}	182.8	275.5	167.6	356.3
d_{max} (mm)	1.8	2.1	1.2	0.8
PIE_{sd} (mm)	12.1	5.5	8.0	4.3

models. In addition, all designs use elastic materials. Current efforts are devoted to extend the current limitation of our topology optimization algorithm and include viscoelastic materials. The effect of mechanism size and density (mechanisms per unit cell) implemented through multiscale topology optimization is also under consideration. In terms of analysis, this work is limited to liner sample simulations; however, a more clear assessment would include simulations and physical verification of a full-sized helmet.

FIGURE 20 Displacement-acceleration and time-acceleration profiles for the EPP foam liner and CML-based PL design with 70A rubber: comparison of 2D and 3D models.
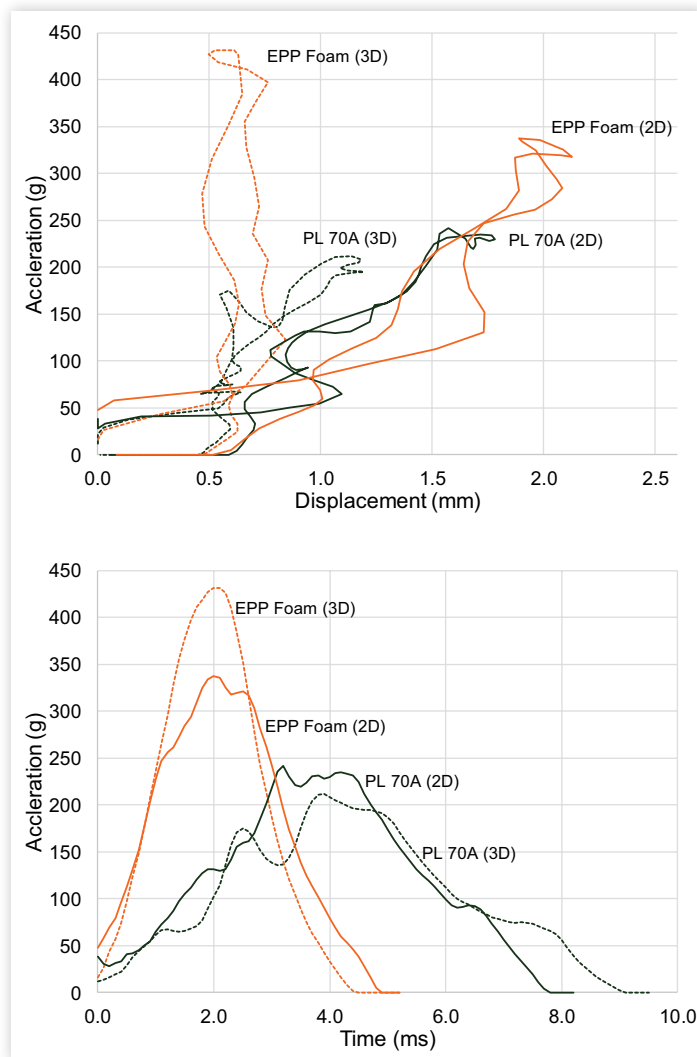
Contact Information

723 W Michigan St, SL 260N, Indianapolis, IN 46202, USA

Acknowledgments

References

1. Mez, J. et al., "Clinicopathological Evaluation of Chronic Traumatic Encephalopathy in Players of American Football," *JAMA* 318(4):360-370, 2017.

2. Collins, M.W. et al., "Cumulative Effects of Concussion in High School Athletes," *Neurosurgery* 51(5):1175-1179, 2002; discussion 1180-1181.

3. B.H.S.I., "Bicycle Helmet Liners: Foam and Other Materials," 2017.

4. Luo, Y. and Liang, Z., "Understanding how a Sport-Helmet Protects the Head from Closed Injury by Virtual Impact Tests," *Bio-Medical Materials and Engineering* 28(3):279-291, 2017.

5. Schwizer, P., Demierre, M., and Smith, L.V., "An Experimental and Numerical Study of Softball to Facemask Impacts," *Proceedings of the Institution of Mechanical Engineers, Part P: Journal of Sports Engineering and Technology* 231(4):336-343, 2017.

6. Teng, T.-L., Liang, C.-C., and Nguyen, V.-H., "Innovative Design of Bicycle Helmet Liners," *Proceedings of the Institution of Mechanical Engineers, Part L: Journal of Materials: Design and Applications* 228(4):341-351, 2014.

7. Soe, S.P. et al., "Mechanical Characterisation of Duraform Flex for FEA Hyperelastic Material Modelling," *Polymer Testing* 34:103-112, 2014.

8. Zhang, Y. and Kwok, T.H., "An Interactive Product Customization Framework for Freeform Shapes," *Rapid Prototyping Journal* 23(6):1136-1145, 2017.

9. Moss, W.C., King, M.J., and Blackman, E.G., "Towards Reducing Impact-Induced Brain Injury: Lessons from a Computational Study of Army and Football Helmet Pads," *Computer Methods in Biomechanics and Biomedical Engineering* 17(11):1173-1184, 2014.

10. Johnson, K.L. et al., "Constrained Topological Optimization of a Football Helmet Facemask Based on Brain Response," *Materials and Design* 111:108-118, 2016.

11. Smith, T.A. et al., "Angular Head Motion with and without Head Contact: Implications for Brain Injury," *Sports Engineering* 18(3):165-175, 2015.

12. Shuaeib, F.M. et al., "A New Motorcycle Helmet Liner Material: The Finite Element Simulation and Design of Experiment Optimization," *Materials and Design* 28(1):182-195, 2007.

13. Halimi, M.T., Hassen, M.B., and Sakli, F., "Design of a Novel Comfort Liner for a Motorcycle Helmet," *International Journal of Sustainable Engineering* 5(2):128-134, 2012.

14. Blanco, D.H., Cernicchi, A., and Galvanetto, U., "Design of an Innovative Optimized Motorcycle Helmet," *Proceedings of the Institution of Mechanical Engineers, Part P: Journal of Sports Engineering and Technology* 228(2):95-110, 2014.

15. Mills, N.J. and Gilchrist, A., "Bicycle Helmet Design," *Proceedings of the Institution of Mechanical Engineers, Part L: Journal of Materials: Design and Applications* 220(4):167-180, 2006.

16. Soe, S.P. et al., "Feasibility of Optimising Bicycle Helmet Design Safety through the Use of Additive Manufactured TPE Cellular Structures," *International Journal of Advanced Manufacturing Technology* 79(9-12):1975-1982, 2015.

17. Johnson, K., "Princeton Schools to Become the First in State to Require Headgear for Soccer, Lacrosse and Field Hockey Players," 2013, http://www.nj.com/mercer/index. ssf/2013/08/princeton_schools_become_the_first_in_the_state_to_require_headgear_ for_soccer_lacrosse_and_field_ho.html.

18. Helmets.org., "Helmets for Many Activities," 2016, http://www.bhsi.org/other.htm.

19. Neurology, A.A.o., "Helmet Add-Ons May Not Lower Concussion Risk in Athletes," 2015, https://www.aan.com/PressRoom/Home/PressRelease/1347.

20. Fu, K. et al., "Bio-Inspired Design: An Overview Investigating Open Questions from the Broader Field of Design-by-Analogy," *Journal of Mechanical Design, Transactions of the ASME* 136(11), 2014.

21. Gibson, L.J. and Ashby, M.F., "Energy Absorption in Cellular Materials," *Cellular Solids: Structure and Properties*, Second Edition (Cambridge, Cambridge University Press, 1997), 309-344.

22. Wang, J. and Rai, R., "Classification of Bio-Inspired Periodic Cubic Cellular Materials Based on Compressive Deformation Behaviors of 3D Printed Parts and FE Simulations," in *28th International Conference on Design Theory and Methodology*, Charlotte, NC, 2016, V007T06A003.

23. Vincent, J.F. and Mann, D.L., "Systematic Technology Transfer from Biology to Engineering," *Philos Trans A Math Phys Eng Sci* 360(1791):159-173, 2002.

24. Tinsley, A. et al., "Exploring the Use of Functional Models as a Foundation for Biomimetic Conceptual Design," in *19th International Conference Design Theory and Methodology* and *1st International Conference Micro and Nano Systems*, Presented at *the 2007 ASME International Design Engineering Technical Conferences and Computers and Information in Engineering Conference*, IDETC/CIE2007, Sept. 4-7, 2007 (Las Vegas, NV: American Society of Mechanical Engineers (ASME), 2008).

25. Nagel, J.K.S., Nagel, R.L., and Eggermont, M., "Teaching Biomimicry with an Engineering-to-Biology Thesaurus," in *ASME 2013 International Design Engineering Technical Conferences and Computers and Information in Engineering Conference, IDETC/ CIE 2013*, American Society of Mechanical Engineers, Portland, OR, Aug. 4, 2013.

26. Chakrabarti, A. et al., "A Functional Representation for Aiding Biomimetic and Artificial Inspiration of New Ideas," *Artificial Intelligence for Engineering Design, Analysis and Manufacturing: AIEDAM* 19(2):113-132, 2005.

27. Vattam, S. et al., *DANE: Fostering Creativity in and through Biologically Inspired Design* (London: Springer, 2011).

28. Srinivasan, V. and Chakrabarti, A., "An Empirical Evaluation of Novelty-Sapphire Relationship," in *2009 ASME International Design Engineering Technical Conferences and Computers and Information in Engineering Conference, DETC2009*, Aug. 30-Sept. 2, 2009 (San Diego, CA, American Society of Mechanical Engineers (ASME), 2010).

29. Buhrig-Polaczek, A. et al., "Biomimetic Cellular Metals - Using Hierarchical Structuring for Energy Absorption," *Bioinspiration and Biomimetics* 11(4), 2016.

30. Looyrach, J. et al., "Pomelo (Citrus Maxima) Peel-Inspired Property for Development of Eco-Friendly Loose-Fill Foam. in *8th International Conference on Materials Science and Technology, MSAT 2014*, Dec. 15-16, 2014 (Bangkok, Thailand, Trans Tech Publications Ltd., 2015).

31. Wang, B., Pan, B., and Lubineau, G., "Morphological Evolution and Internal Strain Mapping of Pomelo Peel Using X-Ray Computed Tomography and Digital Volume Correlation," *Materials and Design* 137:305-315, 2018.

32. Mehta, P.S. et al., "Bio-Inspired Design of Lightweight and Protective Structures," SAE Technical Paper 2016-01-0396, 2016, doi:10.4271/2016-01-0396.

33. Naleway, S.E. et al., "Structural Design Elements in Biological Materials: Application to Bioinspiration," *Advanced Materials* 27(37):5455-5476, 2015.

34. Wang, B. et al., "Keratin: Structure, Mechanical Properties, Occurrence in Biological Organisms, and Efforts at Bioinspiration," *Progress in Materials Science* 76:229-318, 2016.

35. Gibson, L.J., Ashby, M.F., and Harley, B.A., *Cellular Materials in Nature and Medicine* (Cambridge: Cambridge University Press, 2010).

36. Chintapalli, R.K. et al., "Fabrication, Testing and Modeling of a New Flexible Armor Inspired from Natural Fish Scales and Osteoderms," *Bioinspiration and Biomimetics* 9(3):036005, 2014.

37. Wang, L. et al., "Why Do Woodpeckers Resist Head Impact Injury: A Biomechanical Investigation," *PLoS ONE* 6(10):e26490, 2011.

38. Oda, J., Sakamoto, J., and Sakano, K., "Mechanical Evaluation of the Skeletal Structure and Tissue of the Woodpecker and Its Shock Absorbing System," *JSME International Journal, Series A: Solid Mechanics and Material Engineering* 49(3):390-396, 2006.

39. Yoon, S.-H., Roh, J.-E., and Kim, K.L., "Woodpecker-Inspired Shock Isolation by Microgranular Bed," *Journal of Physics D: Applied Physics* 42(3):035501, 2009.

40. Wu, Y. et al., "Dynamic Crash Responses of Bio-Inspired Aluminum Honeycomb Sandwich Structures with CFRP Panels," *Composites Part B: Engineering* 121:122-133, 2017.

41. Jiang, C. et al., "Freeform Honeycomb Structures," *Comput. Graph. Forum* 33(5):185-194, 2014.

42. Schaedler, T.A. et al., "Designing Metallic Microlattices for Energy Absorber Applications," *Advanced Engineering Materials* 16(3):276-283, 2014.

43. Stephani, G. et al., "Iron Based Cellular Structures - Status and Prospects," *Advanced Engineering Materials* 8(9):847-852, 2006.

44. Goehler, H. et al., "Functionalized Metallic Hollow Sphere Structures," *Advanced Engineering Materials* 16(3):335-339, 2014.

45. Li, M.-Z., Stephani, G., and Kang, K.-J., "New Cellular Metals with Enhanced Energy Absorption: Wire-Woven Bulk Kagome (WBK)-Metal Hollow Sphere (MHS) Hybrids," *Advanced Engineering Materials* 13(1-2):33-37, 2011.

46. Tay, Y.Y., Lim, C.S., and Lankarani, H.M., "A Finite Element Analysis of High-Energy Absorption Cellular Materials in Enhancing Passive Safety of Road Vehicles in Side-Impact Accidents," *International Journal of Crashworthiness* 19(3):288-300, 2014.

47. Pinto, P. et al., "Compressive Properties and Energy Absorption of Aluminum Foams with Modified Cellular Geometry," *Journal of Materials Processing Technology* 214(3):571-577, 2014.

48. Schaedler, T.A. and Carter, W.B., "Architected Cellular Materials," *Annual Review of Materials Research* 46:187-210, 2016.

49. Gokhale, V.V. et al., "Design of an Advanced Layered Composite for Energy Dissipation using a 3D-Lattice of Micro Compliant Mechanism," SAE Technical Paper 2016-01-1538, 2016, doi:10.4271/2016-01-1538.

50. Gokhale, V., Tapkir, and Tovar, A., "Force Diverting Helmet Liner Achieved through a Lattice of Multi-Material Compliant Mechanisms," in *ASME 2017 International Design Engineering Technical Conferences and Computers and Information in Engineering Conference, IDETC/CIE 2017*, Aug. 6-9, 2017 (Cleveland, OH: American Society of Mechanical Engineers (ASME)).

51. Najmon, J.C., "Design of Compliant Mechanism Lattice Structures for Impact Energy Absorption," Mechanical Engineering, Purdue University, Indianapolis, 2017.

52. Lu, G. and Yu, T., "Chapter 2: Methodology of Analysing Energy-Absorption Capacities," in *Energy Absorption of Structures and Materials*, Lu, G. and Yu, T., Editors (Woodhead Publishing, 2003), 25-67.

53. Thielen, M., Speck, T., and Seidel, R., "Impact Behaviour of Freeze-Dried and Fresh Pomelo (Citrus Maxima) Peel: Influence of the Hydration State," *Royal Society Open Science* 2(6):140322, 2015.

54. Thielen, M., Schuler, P., and Fischer S.F., "Biomimetic Engineering: Learning from Nature," 2013.

55. Fukuda, Y., "Histology of the Long Digital Tentacles," in *Nautilus: The Biology and Paleobiology of a Living Fossil*, Reprint with Additions, Saunders, W.B. and Landman, N.H., Editors (Dordrecht, the Netherlands, Springer, 2010), 249-256.

56. Liu, K. and Tovar, A., "An Efficient 3D Topology Optimization Code Written in Matlab," *Structural and Multidisciplinary Optimization* 50(6):1175-1196, 2014.

57. Svanberg, K., "The Method of Moving Asymptotes - A New Method for Structural Optimization," *International Journal for Numerical Methods in Engineering* 24(2):359-373, 1987.

58. NOCSAE, "Standard Test Method and Equipment Used in Evaluating the Performance Characteristics of Headgear/Equipment, in Certification of New Equipment," National Operating Committee on Standards for Athletic Equipment, 2017, http://nocsae.org/standards/certification-of-new-equipment/.

59. Hallquist, J.O., *LS-DYNA Theory Manual* (Livermore, CA: Livermore Software Technology Corporation, 2006).

60. Altidis, P., Warner B., and Adams V., "Analyzing Hyperelastic Materials with Some Practical Considerations," IMPACT Engineering Solutions, Inc., 2005.

61. Wohlers, T. and Gornet, T., "History of Additive Manufacturing," 2016.

62. Bouix, R., Viot, P., and Lataillade, J.-L., "Polypropylene Foam Behaviour under Dynamic Loadings: Strain Rate, Density and Microstructure Effects," *International Journal of Impact Engineering* 36(2):329-342, 2009.

63. Gennarelli, T.A. et al., "Directional Dependence of Axonal Brain Injury due to Centroidal and Non-Centroidal Acceleration," SAE Technical Paper 872197, 1987, doi:10.4271/872197.

64. Post, A. et al., "Peak Linear and Rotational Acceleration Magnitude and Duration Effects on Maximum Principal Strain in the Corpus Callosum for Sport Impacts," *Journal of Biomechanics* 61:183-192, 2017.

65. McHenry, B.G., "Head Injury Criterion and the ATB," 2004.

66. Mackay, M., "The Increasing Importance of the Biomechanics of Impact Trauma," *Sadhana* 32(4):397-408, 2007.

67. Saaty, T., Thibault, L., Tomei, G., and Wiser, R., "Relative Measurement and Its Generalization in Decision Making Why Pairwise Comparisons Are Central in Mathematics for the Measurement of Intangible Factors the Analytic Hierarchy/Network Process," *RACSAM - Revista de la Real Academia de Ciencias Exactas, Fisicas y Naturales. Serie A. Matematicas* 102(2):251-318, 2008.

Appendix

LS-DYNA Material Model Keycard Details

Keycard parameters that are not in the table are left at default values. LS-DYNA simulations ran with base units of g, mm, ms.

TABLE A.1 Polycarbonate shell material keycard.

MAT 001-Elastic	RO	E	PR
	0.012	2390	0.37

© Indiana University-Purdue University Indianapolis

TABLE A.2 Impactor material keycard.

MAT 020-Rigid	RO	E	PR	CON1
	0.045	2390	0.37	3

© Indiana University-Purdue University Indianapolis

TABLE A.3 Natural rubber material keycard.

MAT 027-Mooney-Rivlin rubber	Shore A hardness	RO	PR	A	B
	50	0.012	0.4999	0.302	0.076
	60	0.012	0.4999	0.474	0.118
	70	0.012	0.4999	0.736	0.184
	80	0.012	0.4999	1.038	0.260

© Indiana University-Purdue University Indianapolis

TABLE A.4 MEP polyurethane test pad material keycard.

MAT 027-Mooney-Rivlin rubber	RO	PR	A	B
	0.001	0.4999	0.432	0.043

© Indiana University-Purdue University Indianapolis

TABLE A.5 Expanded polypropylene foam material keycard.

MAT 057-Low density foam	RO	E	TC	HU	DAMP	SHAPE
	8.6e−5	1	1e+10	0.2	0.1	5

© Indiana University-Purdue University Indianapolis

Positions and opinions advanced in this work are those of the author(s) and not necessarily those of SAE International. Responsibility for the content of the work lies solely with the author(s).